Materials Horizons

ROYAL SOCIETY OF CHEMISTRY

COMMUNICATION

View Article Online
View Journal | View Issue

Check for updates

Cite this: *Mater. Horiz.*, 2024, 11, 680

Received 2nd October 2023,
Accepted 13th November 2023

DOI: 10.1039/d3mh01597a

rsc.li/materials-horizons

Published on 13 lapkrio 2023. Downloaded on 2025-02-10 08:58:50.

Magnetic assembly of plasmonic chiral superstructures with dynamic chiroptical responses†

Chaolumen Wu, Qingsong Fan, Zhiwei Li, Zuyang Ye and Yadong Yin *

Plasmonic nanostructures exhibiting dynamically tunable chiroptical responses hold great promise for broad applications such as sensing, catalysis, and enantioselective analysis. Despite the successful fabrication of chiral structures through diverse templates, creating dynamic chiroptical materials with fast and reversible responses to external stimuli is still challenging. This work showcases reversible magnetic assembly and active tuning of plasmonic chiral superstructures by introducing a chiral magnetic field from a cubic permanent magnet. Manipulating the strength and direction of the magnetic field controls both the chiral arrangement and plasmonic coupling of the nanoparticle assembly, enabling fast and reversible tunability in not only the handedness of the superstructures but also the spectral characteristics of their chiroptical properties. The dynamic tunability further enables the fabrication of color-changing optical devices based on the optical rotatory dispersion effect, showcasing their potential for application in anti-counterfeiting and stress sensors.

New concepts

In this work, reversible magnetic assembly and active tuning of plasmonic chiral superstructures have been achieved by assembling magneto-plasmonic hybrid nanoparticles within a chiral quadrupole magnetic field from a cubic permanent magnet. Unlike other chiral structures generated using diverse nanoscale templates, this work addresses the challenge of creating dynamic chiroptical materials with fast and reversible responses to external stimuli. The magnetic assembly process not only imparts chirality to the nanoparticle assemblies but also brings them into close proximity, enabling plasmonic coupling and, consequently, the change of their plasmon resonance wavelength. These chiral superstructures exhibit great dynamic tunability in their handedness and the spectral characteristics (circular dichroism magnitude and spectral position) of their chiroptical responses. Furthermore, magnetic assembly and high spectral tunability are combined to create plasmonic chiral films by encompassing the assembled structures within a polymer matrix, showing angular-dependent and mechanically tunable chiroptical properties, including the exciting ability to dynamically change colors through the optical rotatory dispersion (ORD) effect. The chirality of the embedded superstructures can be pre-designed to produce chiral films with desired patterns and switchable colors, promising great potential for application in color displays and anti-counterfeiting measures.

Introduction

Chiral metamaterials are attractive due to their orders of magnitude stronger chiral optical signals than natural chiral species.[1–4] Within them, plasmonic chiral nanostructures have garnered considerable attention for their ability to further enhance chiroptical properties due to strong plasmonic resonance, promising for advanced applications in light-polarization filters, photon detection, molecular sensing, lasers, and chirality tuning.[5–10] While both top-down[11–14] and bottom-up[15,16] methods have been explored for fabricating plasmonic chiral nanostructures, the latter is often favored due to its ease in tuning the size and composition of the building blocks, producing versatile chiral nanostructures endowed with highly controllable chiroptical properties. These methods typically utilize chiral templates such as DNA,[17–19] peptides,[20,21] and chiral fibers[22] to direct the assembly of colloidal plasmonic nanoparticles into chiral nanostructures, thus offering distinct advantages, including the capability for large-scale synthesis and achieving nanoscale resolution. However, many of these methods have encountered challenges in achieving reconfigurable chiral superstructures and responsive chiroptical properties due to the stiffness of the templates, limiting their full potential in real-time applications, such as chiral sensing, catalysis, and enantioselective analysis.[23]

The magnetic assembly approach, known for its fast response, complete reversibility, and remote controllability, has proven effective in assembling magneto-plasmonic nanoparticles into superstructures with dynamically tunable plasmonic properties.[24–32] Its capabilities have recently been expanded to produce plasmonic

Department of Chemistry, University of California, Riverside, CA 92521, USA. E-mail: yadong.yin@ucr.edu

† Electronic supplementary information (ESI) available. See DOI: https://doi.org/10.1039/d3mh01597a

This journal is © The Royal Society of Chemistry 2024

Published on 13 lapkriio 2023. Downloaded on 2025-02-10 08:58:50.

chiral nanostructures featuring dynamic chiroptical tunability by assembling magneto-plasmonic nanoparticles in chiral magnetic fields. Lee *et al.* first demonstrated such an assembly strategy in a helical magnetic field created by positioning two permanent magnets with a twisted angle.[33] Moreover, our recent discovery unveiled inherent quadrupole field chirality generated by a permanent magnet, arising from its consistent field rotation in space.[34] Such chiral fields can be used to assemble magnetic nanoparticles into chiral superstructures, enabling the dynamic tuning of structure handedness and the magnitude of chiroptical signals by controlling the direction and strength of the magnetic field.[21,33] Concurrently, researchers have explored the concept of plasmonic coupling, taking advantage of the close proximity of plasmonic nanoparticles to enhance the tunability of their chiroptical responses.[23] A noteworthy illustration of this concept was recently demonstrated by Fery *et al.*, who showcased the development of mechanically responsive plasmonic chiral nanostructures by stacking two gold nanochain films.[35]

In this work, we present the remarkable tunability of plasmonic chiral superstructures formed by assembling magneto-plasmonic nanoparticles within a chiral quadrupole magnetic field. These structures exhibit great dynamic changes in structural handedness and show fast and reversible chiroptical responses to an external magnetic field by taking advantage of the instant tunability inherent in the magnetic assembly process. When magneto-plasmonic core/shell nanospheres were used as building blocks, one-dimensional nanochains were formed due to the magnetic dipole–dipole interactions between nanospheres, leading to plasmonic coupling and tunable plasmon resonance in the visible spectrum, which further assembled into three-dimensional chiral superstructures driven by the chiral magnetic fields. Combining controllable plasmonic coupling with highly tunable structural handedness enables the design of hierarchical superstructures with widely tunable chiroptical properties. Furthermore, the magnetic assembly method allows fixing the chiral superstructures in photocurable polymer films, during which the structural handedness and chiroptical properties can be precisely controlled in different domains. We report the creation of smart plasmonic chiral films with angular-dependent and mechanically tunable chiroptical properties, demonstrating exciting color switching due to the optical rotatory dispersion (ORD) effect. This magnetic assembly approach to smart chiroptical materials opens up exciting possibilities for applications that demand real-time chiroptical responses, including chiral sensing, enantioselective analysis, and catalysis.

Experimental

Materials

Poly(acrylic acid) (PAA, M_w = 1800), ethylene glycol, iron(III) nitrate nonahydrate ($Fe(NO_3)_3{\cdot}9H_2O$), sodium acetate (NaAc), silver nitride ($AgNO_3$), ammonium hydroxide solution (~28% NH_3 in water), *N*,*N*′-methylenebisacrylamide (BIS), and 2-hydroxy-2-methylpropiophenone (PI) were purchased from Aldrich Chemical Co. Ethanol was obtained from Decon Labs. Acrylamide (AM) was purchased from Acros Organics.

Synthesis of $Ag@Fe_3O_4$ nanoparticles

$Ag@Fe_3O_4$ nanoparticles were synthesized by a solvothermal approach from our previously reported work.[36] Typically, $Fe(NO_3)_3{\cdot}9H_2O$ (1.414 g) was dissolved in ethylene glycol (EG, 35 mL) to form a clear solution, followed by the addition of sodium acetate (NaAc, 2.512 g) and silver nitride ($AgNO_3$, 0.0876 g). The obtained suspension was then transferred to a 45 mL Teflon-lined stainless-steel autoclave, stirred until all the reactants were fully dissolved, and heated at 200 °C for 4 h. The autoclave was allowed to cool down to room temperature naturally. Finally, the black precipitate was magnetically collected and rinsed thoroughly with Milli-Q water and absolute ethanol, followed by dispersion in Milli-Q water.

PAA modification of $Ag@Fe_3O_4$ nanoparticles

One batch of $Ag@Fe_3O_4$ nanoparticles was added to the PAA aqueous solution (50 mg PAA (MW = 1800) in 200 mL water) and stirred overnight at 260 rpm. The sample was collected by centrifugation, washed with Milli-Q water once, and dispersed in 35 mL of Milli-Q water (16 mg mL^{-1}).

Fixing the $Ag@Fe_3O_4$ nanoparticle chains in the polyacrylamide (PAM) film

A magnetic field-assisted photo-polymerization method was used to fix the $Ag@Fe_3O_4$ nanoparticles into chains within the PAM film. Typically, a precursor monomer solution was first prepared by mixing 0.25 g of AM, 4 mg of Bis, and 3 μL of PI in 1 mL of ethylene glycol. Then, 10 μL of the $Ag@Fe_3O_4$ nanoparticle solution (16 mg mL^{-1}) was mixed with 200 μL of precursor solution (nanoparticle concentration in the precursor solution: 0.76 mg mL^{-1}), poured into a template and placed next to a permanent magnet. Afterwards, polymerization was initiated using a UV lamp with a wavelength of 254 nm, producing a chiral plasmonic film with a thickness of 1 mm after 3 minutes.

For creating pre-designed patterns and images, a photomask was placed right above the devices, and then a permanent magnet was applied to align the $Ag@Fe_3O_4$ nanoparticles in the desirable direction. The transparent parts of the photomask enable a high transmittance of UV light to the polymer resin, which will initiate the polymerization and consequently fix the alignment of $Ag@Fe_3O_4$ nanoparticles. Using the sequential orientation–polymerization process, desirable images can be printed by controlling the orientational dispersion of $Ag@Fe_3O_4$ nanoparticles.

Characterization

The morphology of nanostructures was investigated using a Thermo Scientific™ Talos L120C™ TEM. The optical extinction and transmission spectra were measured using an Ocean Insight FLAME-T-UV-VIS Miniature Spectrometer. The CD spectra were measured on a Jasco J-815 CD spectrophotometer. The concentration of the nanoparticle solution for optical

Published on 13 lapkriio 2023. Downloaded on 2025-02-10 08:58:50.

measurement is 0.80 mg mL^{-1}. All the photos and videos were recorded using a Canon EOS REBEL T2i camera.

Results and discussion

A quadrupole chiral magnetic field can be generated using a cubic permanent magnet due to constant field rotation.[34] Fig. 1a and Fig. S1a (ESI†) show the simulated chiral magnetic field, with left- and right-handed chiral magnetic fields from the right and left sides of the cubic magnet. When the nanoparticles are assembled under such chiral magnetic fields, the field chirality can be transferred to the nanoparticle assemblies, producing chiral nanostructures (Fig. 1a). In this work, we employed magneto-plasmonic Ag@Fe_3O_4 core–shell nanoparticles as building blocks, each featuring a core diameter of ~80 nm and a shell thickness of ~75 nm (Fig. 1b and Fig. S0, ESI†). By taking advantage of their strong interaction with both light and magnetic fields, we showcase their assembly into plasmonic chiral superstructures under the chiral magnetic field. The nanoparticles were first assembled into one-dimensional nanochains due to magnetic dipole–dipole interaction. Simultaneously, these nanochains were organized into chiral arrangements driven by the chiral magnetic field (Fig. S1b, ESI†). Fig. 1c shows the experimental setup for measuring the extinction and CD spectra. A cubic magnet was placed beside the sample (nanoparticle dispersion enclosed in a cuvette), and the magnetic field direction was controlled by rotating the magnet. Fig. 1d shows the extinction spectra of the Ag@Fe_3O_4 nanoparticle dispersion in the absence of a magnetic field or with a magnetic field applied along the *X*- (B_x) and *Z*-axes (B_z). Both dipole and quadrupole peaks blue-shifted under B_x and B_z due to far-field plasmonic coupling.[36] Fig. 1e presents the CD spectra of the nanoparticle dispersion, both without a magnetic field and when assembled under magnetic fields B_x and B_z. The Ag@Fe_3O_4 nanoparticles themselves were achiral and exhibited no CD signal. In contrast, when they were magnetically assembled, an obvious CD signal emerged, characterized by a bisignate lineshape stemming from dipole and quadrupole plasmonic peaks. We defined the peak around 666 nm as a dipole CD peak and the one around 460 nm as a quadrupole CD peak. As shown in Fig. 1e, the CD signal was reversed while maintaining the magnitude upon switching the magnetic field from B_x to B_z, indicating the handedness switch of the chiral superstructures. Fig. 1f shows the corresponding *g*-factor of the nanoparticle assemblies, with a maximum *g*-factor value reaching ±0.01, which indicates the strong chirality of the assembled plasmonic chiral superstructures.

The direction of the magnetic field influences the plasmonic chiroptical properties due to the angular-dependent plasmonic coupling and chirality field distribution. As shown in Fig. 2a, the angle between the north pole of the magnet and incident light direction was defined as α, and it varied from 0 to 90°

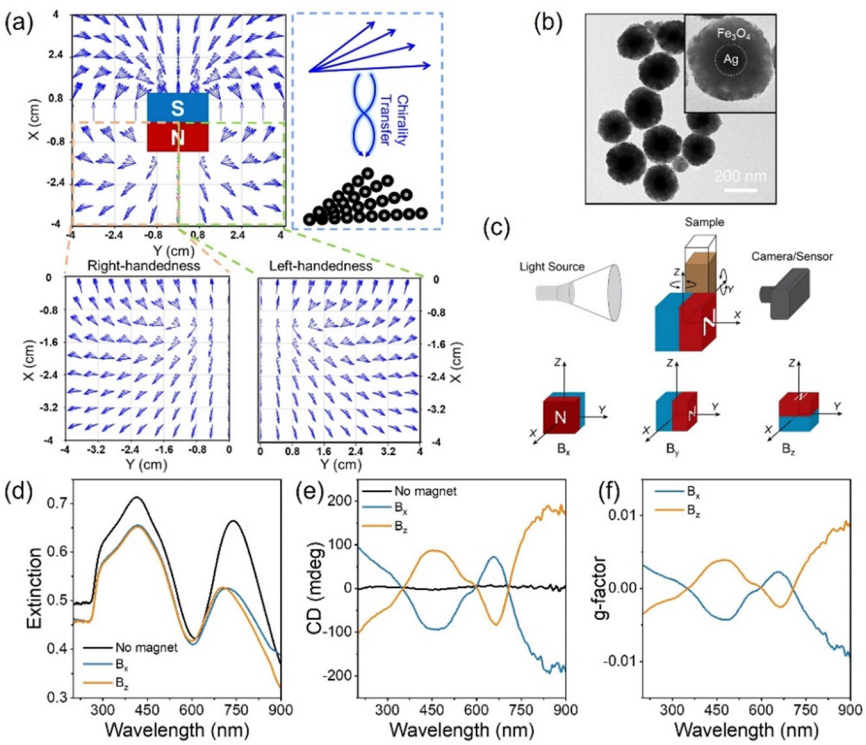

Fig. 1 (a) Simulation of the chiral field distribution from a cubic permanent magnet and schematic illustration of the chirality transfer from a chiral magnetic field to magnetic nanoparticle assembly. (b) TEM image of Ag@Fe_3O_4 hybrid nanoparticles. (c) Schematic illustration of the setup for measuring the extinction and CD spectrum of particle dispersion under a chiral magnetic field. (d)–(f) Extinction (d), CD (e), and the corresponding *g*-factor (f) spectra of the Ag@Fe_3O_4 nanoparticle dispersion without a magnetic field or under a field along the *X*- and *Z*-axes.

 This journal is © The Royal Society of Chemistry 2024

Published on 13 lapkrio 2023. Downloaded on 2025-02-10 08:58:50.

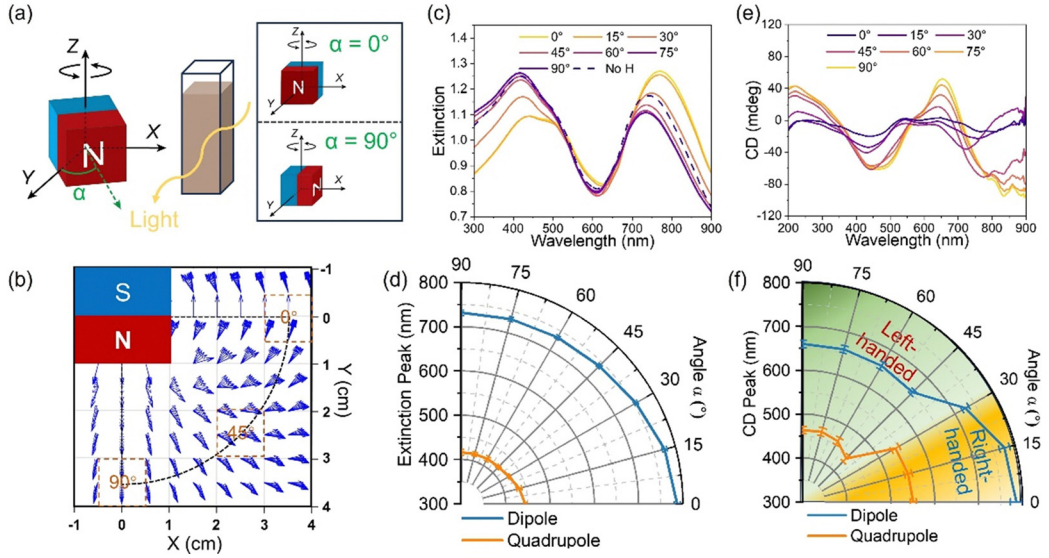

Fig. 2 (a) A scheme illustrating the field rotation of a cubic magnet along the *Z*-axis within the *XY*-plane. (b) Simulation of magnetic field distribution as the north pole rotated from the *X*-axis (90°) to the *Y*-axis (0°). (c) and (d) Extinction spectra and the corresponding dipole and quadrupole peak shifts of the Ag@Fe_3O_4 nanoparticle assemblies upon varying the field from B_x to B_y. (e) and (f) CD spectra and the corresponding dipole and quadrupole peak shifts of the assemblies upon varying the field from B_x to B_y.

when the cubic magnet was rotated from the *Y*-axis to the *X*-axis. The magnetic field distribution within the *XY* plane was simulated, exhibiting a single handedness as α varied from 0 to 90° (Fig. 2b). The nanoparticles assembled under such a field showed an angular-dependent plasmonic coupling (Fig. 2c and d). When α varied from 0 to 45°, the dipole and quadrupole peaks blue-shifted from ~787 to ~740 nm and ~444 to ~418 nm, respectively, but not much changes were observed as α increased from 45° to 90°. As we revealed previously,[36] far-field coupling of the neighboring Ag@Fe_3O_4 nanoparticles could be induced when the magnetic field direction was perpendicular to the incident light (α = 90°), resulting in a blue-shift of the plasmonic peaks. In contrast, the plasmonic peaks red-shifted due to the near-field plasmonic coupling as the magnetic field direction was parallel to the incident light (α = 0°).

Fig. 2e shows the CD spectra of the nanoparticle dispersion while varying α from 0 to 90°. As α increased from 0 to 30°, the dipole and quadrupole CD peaks gradually blue-shifted. Notably, the sign of the CD peaks was flipped when α was 30°, indicating a handedness switch. According to the simulation in Fig. 2b, the handedness of the chiral field was always left-handed when α is 0 to 90°. Thus, the chirality switching of the assembled chiral nanostructures was not induced by the handedness switch of the magnetic field. It has been pointed out that the handedness of a chiral structure also depends on the direction in which it is viewed.[37] Liedl *et al.* also found the switchable CD spectrum of DNA-origami-scaffolded nanoparticle helices by controlling the helix orientation from parallel to perpendicular with respect to the light beam.[38] In our case, the assembled chiral nanostructures showed left-handedness as α was off from the incident light (30–90°), while the handedness was reversed when the chiral nanostructures were aligned along the incident light (0–30°). Fig. 2f shows the handedness switching and the blue-shifting of the dipole and quadrupole CD peaks from 786 to 660 nm and 551 to 463 nm as α varied from 0 to 90°. The intensity of both dipole and quadrupole CD peaks gradually increased as α increased from 0 to 30°. When α varied from 45 to 90°, the dipole CD peak intensity gradually increased, while the quadrupole CD peak intensity showed not much change. Fig. S2 (ESI†) shows the simulation of the rotation of the chiral magnetic field (helix angle) at varying α. With increasing α, the helix angle gradually increased, while it slightly decreased as α varied from 45 to 86°. According to the relationship between pitch (P) and helix angle (θ), $P = \pi D \tan(90 - \theta)$, with D being the diameter of the helical circle, the shorter the pitch, the larger the chirality asymmetry, and the stronger the CD intensity. Furthermore, the angular-dependent plasmonic coupling of the assembled chiral nanostructures also contributed to the change in the CD intensity. These two combined effects contributed to the change in CD magnitude as α varied from 0 to 90°.

Both CD intensity and spectral position can be dynamically tuned by modulating the plasmonic coupling and magnetic field chirality distribution by controlling the magnetic field strength. The magnetic field strength was tuned by the distance between the sample and the cubic magnet, and the shorter the separation distance, the stronger the magnetic field strength. The separation between neighboring nanoparticles was determined by electrostatic repulsion and magnetic attraction. Increasing magnetic field strength decreases the separation distance, enhancing the plasmonic coupling. As shown in Fig. 3a and b, the CD dipole peak gradually blue-shifted, and the CD quadrupole peak slightly red-shifted under increasing B_x intensity. At α = 90°, the electric dipole is perpendicular to the chain, which induces the high energy state of the chain, blue-shifting the plasmonic dipole resonance, while the electric

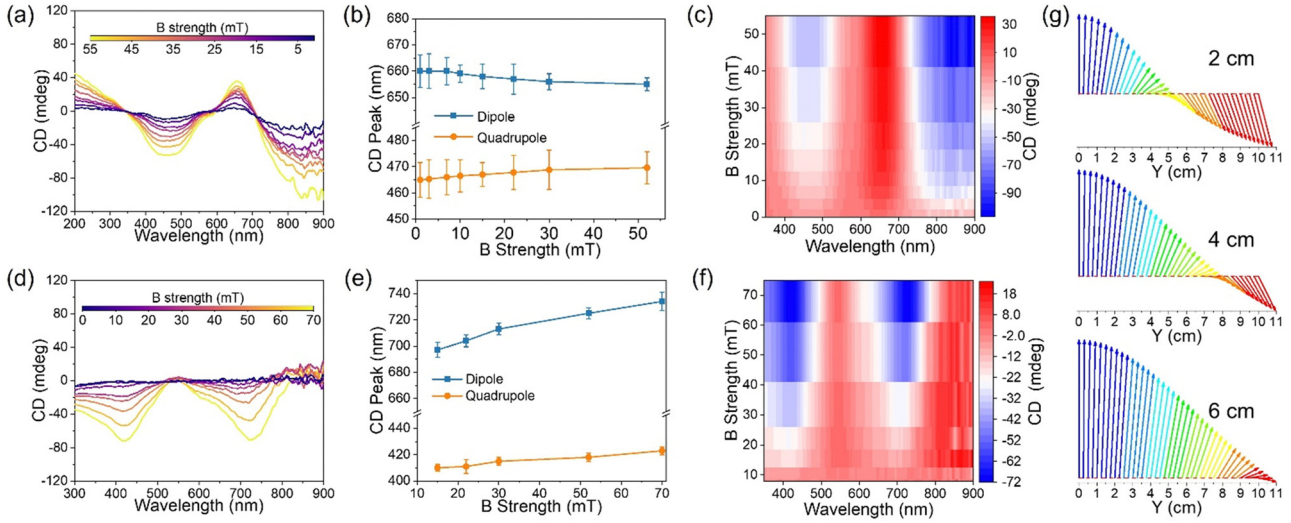

Fig. 3 (a)–(f): CD spectra (a) and (d), the corresponding dipole and quadrupole peak shifts (b) and (e), and the peak intensity changes (c) and (f) of Ag@Fe_3O_4 nanoparticle assembly under B_x and B_y with varying strengths. (g) Simulated magnetic field vector rotation along the *Y*-axis under different distances (2, 4, 6 cm) along the *X*-axis from the magnet, showing that chirality decreases with increasing separation distance.

Published on 13 lapkrio 2023. Downloaded on 2025-02-10 08:58:50.

quadrupoles couple to induce the near field coupling, red-shifting the plasmonic quadrupole resonance.[36] The intensity of dipole and quadrupole peaks was greatly enhanced as B_x strength increased from 1 to 52 mT (Fig. 3c). Under B_y, both CD dipole and quadrupole peaks red-shifted (Fig. 3d and e), and the intensity of both peaks was dramatically enhanced (Fig. 3f) as the magnetic field strength increased from 3 to 70 mT. CD spectrum measures the extinction difference of the chiral superstructures under exciation of left- and right-hand circularly polarized light. Thus, the extinction peak shift directly contributes to the CD peak shift, and they show similar trends (Fig. S3, ESI†). Increasing magnetic field strength enhances the plasmonic coupling, which, in turn, induces both extinction and CD peak shifts. Besides, the chirality of the assembled superstructures also depends on the distance from the magnet. Fig. 3g shows the simulated magnetic field vector rotation along the *Y*-axis at different distances from the cubic magnet along the *X*-axis. With the increase of the distance from the magnet along the *Y*-axis, the magnetic field vector rotates clockwise. The rotation angle depends on the distance on the *X*- and *Y*-axes. We fixed the distance along the *Y*-axis to 10 cm and compared the rotation angle at different distances on the *X*-axis. It was obvious that the rotation angle gradually decreased with the increasing distance along the *X*-axis from 2 to 4 and 6 cm, indicating the increase of the pitch and the decrease of the chirality. Both enhanced plasmonic coupling and pitch decrease contributed to the CD spectral shifts and intensity enhancement under increasing magnetic field strengths.

Because of the ORD effect, the plasmonic chiral superstructures can show distinguishable color switching in response to polarization state changes. Fig. 4a schematically illustrates the experimental setup of the ORD measurement of the Ag@Fe_3O_4 nanoparticle dispersion under a chiral magnetic field. White light initially passes through polarizer 1, becoming a linearly polarized light. Subsequently, the polarization state of the light undergoes alterations as it interacts with the chiral superstructures. Finally, the polarized light of a specific wavelength passes through polarizer 2, displaying a distinct color. We define the angle between two polarizers as β, where a value of 0 corresponds to the two polarizers being orthogonal. While fixing polarizer 1, we rotated polarizer 2 clockwise (+) or anticlockwise (−) to show different colors. Fig. 4b shows the ORD images of the nanoparticle dispersion both in the absence of a magnetic field and when assembled under magnetic fields B_x and B_z. The dispersion exhibited no color without a magnetic field due to a lack of chirality. In contrast, under B_x, the dispersion showed a vivid color change from purple to pink and yellow as β varied from 0 to −10.5°, and from purple to blue and light blue as β increased from 0 to 10.5°. The situation was reversed under B_z due to the handedness switch. Fig. 4c shows the transmission spectra of the nanoparticle dispersion under B_x as β varied from 0 to −13.5° (i) and 0 to 13.5° (ii). When β was negative, the dispersion color generated from the transmitted light with a wavelength of around 750 nm, and it blue-shifted as β varied from 0 to −13.5°. The transmitted light with a wavelength of around 500 nm contributed to the dispersion color when β was positive, and the transmission peak also blue-shifted when β increased from 0 to 13.5°. The dispersion color depends on the chirality of the assembled nanostructures, and it can be dynamically controlled by both the direction and strength of the magnetic fields. Fig. S4 (ESI†) shows the ORD images of the dispersion color at varying α values from 0 to 90°. When β was negative, for example −4.5°, the color gradually changed from pink to blue as α decreased from 90 to 0°. When β was 4.5°, the color changed from light blue to purple when α varied from 90 to 0°. Fig. S5 (ESI†) depicts the effect of the magnetic field strength on the dispersion color. The nanoparticle dispersion exhibited brighter colors with increasing magnetic field strength due to the enhanced chirality under stronger magnetic fields.

 This journal is © The Royal Society of Chemistry 2024

Published on 13 lapkriio 2023. Downloaded on 2025-02-10 08:58:50.

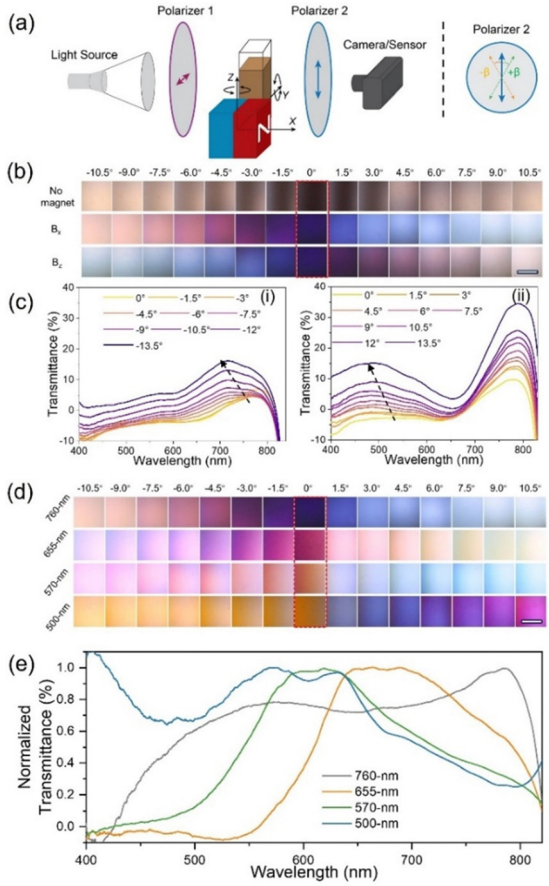

Fig. 4 (a) Schematic illustration of ORD measurement setup. (b) ORD images of Ag@Fe_3O_4 nanoparticle dispersion under no magnetic field or B_x and B_z fields. (c) The transmission spectra of the nanoparticle dispersion under B_x with varying negative (i) and positive (ii) β values. (d) ORD images of Ag@Fe_3O_4 nanoparticles with 760, 655, 570, and 500 nm extinction peaks under B_x with varying β values from −10.5 to 10.5°. (e) The corresponding transmission spectra of the sample in (d) at β = 0°. All the digital images in (b) and (d) share the same scale bar of 1 mm.

The core–shell nanoparticles offer a high degree of control over their plasmonic resonance based on their core size and shell thickness, thereby imparting a wide range of distinctive colors to their chiral superstructures. In addition to the Ag@Fe_3O_4 nanoparticles with dipole extinction peak at 760 nm, three other Ag@Fe_3O_4 nanoparticles with dipole resonance peaks at 655, 570, and 500 nm were synthesized and used as building blocks. Fig. S6 (ESI†) shows their TEM images, extinction spectra without a magnet field, and CD spectra of their assemblies under B_x and B_z. With the blue-shifting of the extinction peaks of the building blocks, the CD peaks were also blue-shifted, showing different CD profiles. Fig. 4d shows the color changes of the above four different nanoparticle dispersions under B_x with β varying from −10.5 to 10.5°. At β = 0°, the dispersions of 760, 655, 570, and 500 nm nanoparticles appeared blue, pink, reddish, and yellow. The transmission spectra showed the transmission peaks of the four samples at β = 0°, indicating the origin of their different colors. The above results underscore the unique advantage of the current system in generating a diverse spectrum of colors in solution, achieved through convenient control over factors such as polarization angle, magnetic field strength and direction, and the structural configuration of Ag@Fe_3O_4 nanoparticles.

The plasmonic chiral superstructures can be fixed inside a polymer matrix through photo-initiated polymerization of monomers added to their dispersion, producing a plasmonic chiral film with tunable chiral optical properties (Fig. 5a(i)). The magnet's north pole was aligned along the *Y*-axis when fixing the nanoparticle assembly in the matrix. Fig. 5a(ii) shows the image of the chiral film with a brownish color under ordinary light. The handedness of the film can be switched by rotating the film, showing left- or right-handedness as the long-axis of the film aligning along the *Y*- or *Z*-axis and light incident along the *X*-axis, which is the same result as applying B_x and B_z. Fig. 5b shows the CD spectra of the chiral film with switchable handedness when rotating the film from the *Y*- to *Z*-axis. Fig. 5c shows the ORD images of the chiral film with tunable colors by varying β from −10.5 to 10.5°, displaying color switching when the film orientation changed from the *Y*-axis to the *Z*-axis. Thanks to the convenience of the magnetic assembly process, color-changing anti-counterfeiting devices could be fabricated by fixing the chiral nanostructures with pre-designed handedness in a polymer matrix. As shown in the scheme in Fig. 5d, the white areas contained left-handed chiral nanostructures, and the black areas contained right-handed chiral nanostructures. They showed no difference at β = 0°, while the white areas appeared orange and black areas appeared blue at β = −4.5°. The colors in black and white regions were reversed at β = 4.5°. As shown in Fig. S7 (ESI†), by using different building blocks, chiral films with different patterns were fabricated and showed different switchable colors, indicating their potential for anti-counterfeiting applications.

The plasmonic chiral film also features angular-dependent colors, which can be controlled by modulating the angle between the film and incident light. Fig. 5e shows the ORD images of the chiral film at β = ±1.5° as the tilting angle between incident light and film varied from 90 to 15° within the *YZ* plane. The color changes from pink to light blue at β = −1.5° and blue to purple at β = 1.5°. Fig. 5f and g show the corresponding transmission spectra of the chiral film at β = ±1.5°. In both cases, the transmission peaks red-shifted as the tilting angle varied from 90° to 15°, consistent with the solution case of varying α from 90 to 0°. The extinction peak of the chiral film also red-shifted as the tilting angle decreased from 90 to 15° (as shown in Fig. S8a, ESI†) due to the angular-dependent plasmonic coupling.

An additional intriguing aspect of the chiral film is its capacity for mechanical tuning of its chiroptical properties, an important property for developing novel stress sensors. As illustrated in the example in Fig. 5h, we designed a chiral film with the middle area containing chiral nanostructures orientated along 45° relative to the long axis of the film while the chiral nanostructures were aligned along the long axis of the film in the remaining area. Under no mechanical stress, they displayed colors of blue and pink, respectively, at β = −1.5°.

Published on 13 lapkriio 2023. Downloaded on 2025-02-10 08:58:50.

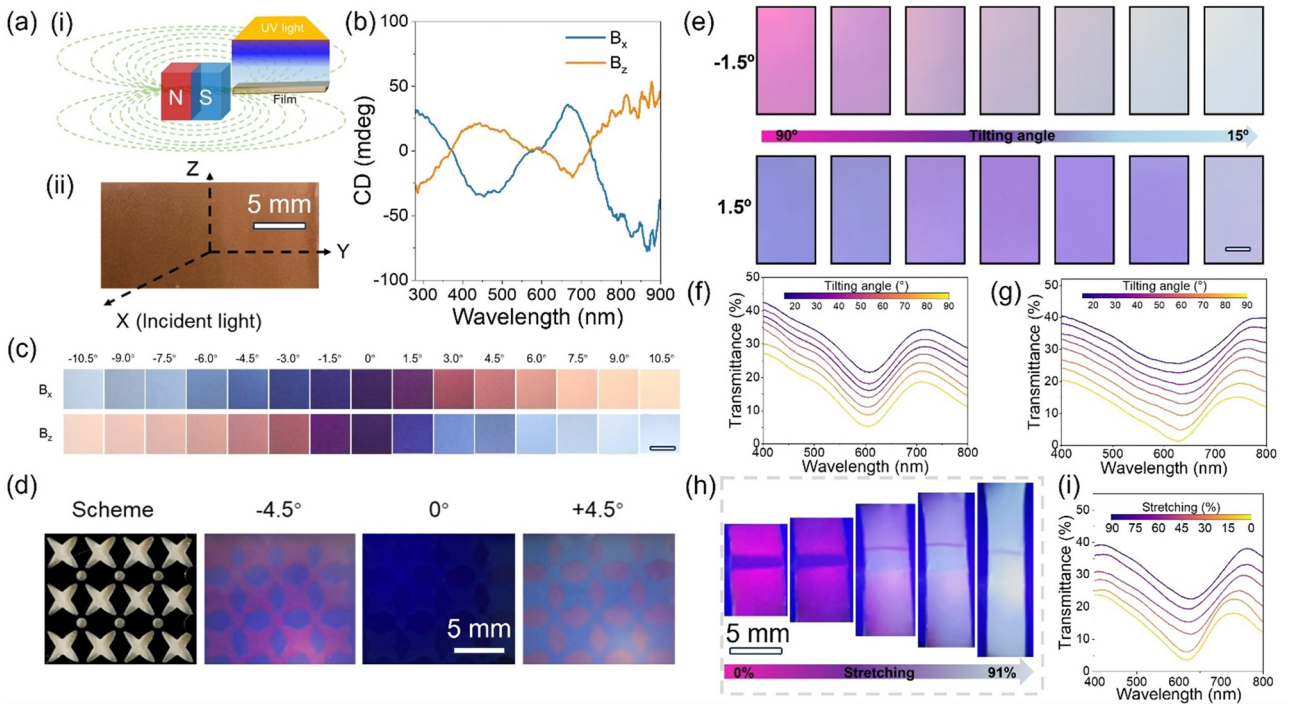

Fig. 5 (a) Scheme illustrating the fixing of plasmonic chiral superstructures in a polymer film (i) and photo of the assembled chiral film (ii). (b) CD spectra of the chiral film with left- and right-handedness. (c) ORD images of the left- and right-handed chiral film under varying β values from −10.5 to 10.5°. (d) Scheme and ORD images of a chiral film pattern with left-handed chiral nanostructures in white regions and right-handed chiral nanostructures in black regions as β = 0 and ±4.5°. (e)–(g) ORD images of the chiral film as the angle between light direction and film varied from 90 to 15° at β = ±1.5° (e) and the corresponding transmission spectra at β = −1.5° (f) and β = 1.5° (g). (h) and (i) ORD images of the chiral film under stretching from 0 to 91% as β = −1.5° (h) and the corresponding transmission spectra (i). All the digital images in figures (c) and (e) share the same scale bar of 1 mm.

Upon stretching from 0 to 92%, both regions gradually turned into light blue, showing no detectable color difference between these two regions. The color changes are consistent with the red-shift of the transmission peak of the pink region under stretching (Fig. 5i). As shown in Fig. S8b and c (ESI†), both plasmonic and CD peaks red-shifted under stretching due to increased separation between neighboring nanoparticles, which decreased the far-field plasmonic coupling and induced the red-shift. Also, the CD intensity gradually decreased with the increase of stress, which may be caused by decreased nanoparticle density and disorder of the chiral nanostructures under stretching. The color of the chiral film can be dynamically controlled by mechanical stress, showcasing the potential for application in stress sensors.

Conclusions

In summary, we showcase here the reversible assembly and active tuning of plasmonic chiral superstructures by assembling Ag@Fe_3O_4 magneto-plasmonic hybrid nanoparticles under a chiral magnetic field. This approach enables the dynamic control of the handedness of the chiral superstructures and the magnitude of their CD response through the convenient manipulation of the magnetic field. In addition, the magnetic assembly process induces plasmonic coupling among the hybrid nanoparticles, facilitating magnetic tuning of the CD spectral position. By utilizing both magnetic field strength and direction to manipulate plasmonic coupling and chirality, one can achieve precise control over the chiroptical properties of plasmonic chiral superstructures. Furthermore, through meticulous control of the core–shell configuration of the hybrid nanoparticles, one can position their plasmonic resonance within the visible spectrum, allowing the chiral superstructures to exhibit vibrant and tunable colors resulting from the ORD effect. These distinctive attributes, coupled with the unique advantages of the magnetic assembly approach, such as convenience, remarkable tunability, and remote operation, have been harnessed to fabricate plasmonic chiral films that feature both angular-dependent and mechanically tunable chiroptical properties. The chirality of the embedded superstructures can be pre-designed to produce chiral films with desired patterns and switchable colors, promising great potential for application in color displays and anti-counterfeiting measures.

Author contributions

Y. Y. and C. W. conceived the idea. C. W. designed and conducted the experiments. Q. F. did the simulation. Z. L. and Z. Y. helped with the data analysis. C. W. wrote the manuscript. Y. Y., Z. L., Z. Y. and Q. F. reviewed and edited the manuscript.

 This journal is © The Royal Society of Chemistry 2024

Published on 13 lapkriio 2023. Downloaded on 2025-02-10 08:58:50.

Conflicts of interest

There are no conflicts to declare.

Acknowledgements

We are grateful for the financial support from the U.S. National Science Foundation (CHE-2203972).

References

1 Z. Ma, Y. Li, Y. Li, Y. Gong, S. A. Maier and M. Hong, *Opt. Express*, 2018, **26**, 6067–6078.
2 Z. Han, F. Wang, J. Sun, X. Wang and Z. Tang, *Adv. Mater.*, 2023, **35**, 2206141.
3 Z. Wang, Y. Wang, G. Adamo, B. H. Teh, Q. Y. S. Wu, J. Teng and H. Sun, *Adv. Opt. Mater.*, 2016, **4**, 883–888.
4 K. Koshelev, S. Lepeshov, M. Liu, A. Bogdanov and Y. Kivshar, *Phys. Rev. Lett.*, 2018, **121**, 193903.
5 X. Lan and Q. Wang, *Adv. Mater.*, 2016, **28**, 10499–10507.
6 Y. Luo, C. Chi, M. Jiang, R. Li, S. Zu, Y. Li and Z. Fang, *Adv. Opt. Mater.*, 2017, **5**, 1700040.
7 W. Jiang, Z.-B. Qu, P. Kumar, D. Vecchio, Y. Wang, Y. Ma, J. H. Bahng, K. Bernardino, W. R. Gomes and F. M. Colombari, *Science*, 2020, **368**, 642–648.
8 J. Lu, Y. Xue and N. A. Kotov, *Isr. J. Chem.*, 2021, **61**, 851–862.
9 N. A. Kotov, L. M. Liz-Marzan and P. S. Weiss, *ACS Nano*, 2021, **15**, 12457–12460.
10 F. Freire-Fernández, J. Cuerda, K. S. Daskalakis, S. Perumbilavil, J.-P. Martikainen, K. Arjas, P. Törmä and S. van Dijken, *Nat. Photonics*, 2022, **16**, 27–32.
11 M. Manoccio, M. Esposito, A. Passaseo, M. Cuscunà and V. Tasco, *Micromachines*, 2020, **12**, 6.
12 J. K. Gansel, M. Latzel, A. Frölich, J. Kaschke, M. Thiel and M. Wegener, *Appl. Phys. Lett.*, 2012, **100**, 101109.
13 J. Kaschke and M. Wegener, *Opt. Lett.*, 2015, **40**, 3986–3989.
14 A. G. Mark, J. G. Gibbs, T.-C. Lee and P. Fischer, *Nat. Mater.*, 2013, **12**, 802–807.
15 D. Vila-Liarte, N. A. Kotov and L. M. Liz-Marzán, *Chem. Sci.*, 2022, **13**, 595–610.
16 M. Hentschel, M. Schäferling, X. Duan, H. Giessen and N. Liu, *Sci. Adv.*, 2017, **3**, e1602735.
17 A. Kuzyk, R. Schreiber, Z. Fan, G. Pardatscher, E.-M. Roller, A. Högele, F. C. Simmel, A. O. Govorov and T. Liedl, *Nature*, 2012, **483**, 311–314.
18 X. Shen, C. Song, J. Wang, D. Shi, Z. Wang, N. Liu and B. Ding, *J. Am. Chem. Soc.*, 2012, **134**, 146–149.
19 X. Lan, Z. Chen, G. Dai, X. Lu, W. Ni and Q. Wang, *J. Am. Chem. Soc.*, 2013, **135**, 11441–11444.
20 J. Lu, Y. Xue, K. Bernardino, N.-N. Zhang, W. R. Gomes, N. S. Ramesar, S. Liu, Z. Hu, T. Sun and A. F. de Moura, *Science*, 2021, **371**, 1368–1374.
21 C. Song, M. G. Blaber, G. Zhao, P. Zhang, H. C. Fry, G. C. Schatz and N. L. Rosi, *Nano Lett.*, 2013, **13**, 3256–3261.
22 A. Guerrero-Martínez, B. Auguié, J. L. Alonso-Gómez, Z. Džolić, S. Gómez-Graña, M. Žinić, M. M. Cid and L. M. Liz-Marzán, *Angew. Chem., Int. Ed.*, 2011, **50**, 5499–5503.
23 F. Neubrech, M. Hentschel and N. Liu, *Adv. Mater.*, 2020, **32**, 1905640.
24 Z. Li, Q. Fan, C. Wu, Y. Li, C. Cheng and Y. Yin, *Nano Lett.*, 2020, **20**, 8242–8249.
25 Z. Li, J. Jin, F. Yang, N. Song and Y. Yin, *Nat. Commun.*, 2020, **11**, 1–11.
26 J. Goebl, Y. Liu, S. Wong, S. Zorba and Y. Yin, *Nanoscale Horiz.*, 2016, **1**, 64–68.
27 M. Wang, C. Gao, L. He, Q. Lu, J. Zhang, C. Tang, S. Zorba and Y. Yin, *J. Am. Chem. Soc.*, 2013, **135**, 15302–15305.
28 Q. Fan, Z. Li, C. Wu and Y. Yin, *Precision Chem.*, 2023, **1**, 272–298.
29 Z. Ye, Z. Li, J. Feng, C. Wu, Q. Fan, C. Chen, J. Chen and Y. J. A. N. Yin, *ACS Nano*, 2023, **17**, 18517–18524.
30 C. Wu, *Doctoral dissertation*, University of California, Riverside, 2023.
31 Z. Li, Q. Fan and Y. J. C. R. Yin, *Chem. Rev.*, 2021, **122**, 4976–5067.
32 Q. Fan, Z. Li and Y. Yin, in *Encycleopedia of Nanomaterials*, ed. Y. Yin, Y. Lu, Y. Xia, Elseviever, Oxford, 2023, **3**, pp. 65–78.
33 K.-J. Jeong, D. K. Lee, V. T. Tran, C. Wang, J. Lv, J. Park, Z. Tang and J. Lee, *ACS Nano*, 2020, **14**, 7152–7160.
34 Z. Li, Q. Fan, Z. Ye, C. Wu, Z. Wang and Y. Yin, *Science*, 2023, **380**, 1384–1390.
35 P. T. Probst, M. Mayer, V. Gupta, A. M. Steiner, Z. Zhou, G. K. Auernhammer, T. A. König and A. Fery, *Nat. Mater.*, 2021, **20**, 1024–1028.
36 C. Wu, Q. Fan, W. Wu, T. Liang, Y. Liu, H. Yu and Y. Yin, *Nano Lett.*, 2023, **23**, 1981–1988.
37 E. Efrati and W. T. Irvine, *Phys. Rev. X*, 2014, **4**, 011003.
38 R. Schreiber, N. Luong, Z. Fan, A. Kuzyk, P. C. Nickels, T. Zhang, D. M. Smith, B. Yurke, W. Kuang and A. O. Govorov, *Nat. Commun.*, 2013, **4**, 1–6.